

Highly efficient and selective electrocatalytic hydrogen peroxide production on Co-O-C active centers on graphene oxide

Bin-Wei Zhang¹, Tao Zheng², Yun-Xiao Wang³, Yi Du³, Sheng-Qi Chu⁴, Zhenhai Xia², Rose Amal¹, Shi-Xue Dou³ & Liming Dai¹✉

Electrochemical oxygen reduction provides an eco-friendly synthetic route to hydrogen peroxide (H₂O₂), a widely used green chemical. However, the kinetically sluggish and low-selectivity oxygen reduction reaction (ORR) is a key challenge to electrochemical production of H₂O₂ for practical applications. Herein, we demonstrate that single cobalt atoms anchored on oxygen functionalized graphene oxide form Co-O-C@GO active centres (abbreviated as Co₁@GO for simplicity) that act as an efficient and durable electrocatalyst for H₂O₂ production. This Co₁@GO electrocatalyst shows excellent electrochemical performance in O₂-saturated 0.1 M KOH, exhibiting high reactivity with an onset potential of 0.91 V and H₂O₂ production of 1.0 mg cm⁻² h⁻¹ while affording high selectivity of 81.4% for H₂O₂. Our combined experimental observations and theoretical calculations indicate that the high reactivity and selectivity of Co₁@GO for H₂O₂ electrogeneration arises from a synergistic effect between the O-bonded single Co atoms and adjacent oxygen functional groups (C-O bonds) of the GO present in the Co-O-C active centres.

¹Australian Carbon Materials Centre (A-CMC), School of Chemical Engineering, The University of New South Wales Sydney, Sydney, NSW 2052, Australia. ²Department of Materials Science and Engineering, Department of Chemistry, University of North Texas, Denton, TX 76203, USA. ³Institute for Superconducting and Electronic Materials, Australian Institute of Innovative Materials, University of Wollongong, Innovation Campus, Squires Way, North Wollongong, NSW 2500, Australia. ⁴Beijing Synchrotron Radiation Facility, Institute of High Energy Physics, Chinese Academy of Sciences, Beijing 100049, People's Republic of China. ✉email: l.dai@unsw.edu.au

Hydrogen peroxide (H_2O_2) as one of the 100 most important chemicals in the world is widely used for various chemical and biological processes, including chemical and pharmaceutical production, environmental protection, and energy storage and conversion^{1,2}. Currently, large-scale infrastructures and tedious multi-step processes are used for industrial production of H_2O_2 at a high temperature and pressure, thereby cost-intensive and rich with sewage by-product^{3–6}. Thus, cost-effective and eco-friendly production of H_2O_2 is highly demanded^{7–9}. In this context, the electrosynthesis of H_2O_2 through oxygen reduction reaction (ORR) via a two-electron pathway has recently attracted significant attention^{10–14}. In particular, considerable effort has been made to enhance the activity and selectivity of electrocatalysts for the electrochemical production of H_2O_2 ^{15,16}. However, the sluggish reactivity and low selectivity are still two obstacles for efficient electrosynthesis of H_2O_2 via the two-electron pathway of oxygen reduction.

Owing to their low coordination environment and high catalytic performance, carbon-based single-metal-atom catalysts (SACs) have recently attracted much attention for electrocatalysis^{17–21}. In most SACs, however, single atoms are anchored on an N-doped carbon support to prevent migration of the metal atoms^{22,23}, which usually lead to the four-electron pathway toward ORR^{24,25}. Therefore, they are not ideal for electrosynthesis of H_2O_2 , which requires a two-electron pathway toward ORR (i.e., 2e ORR)^{26–30}. Compared to N-doped carbon materials, several oxygen functional groups, including COOH and C-O-C, in oxidized carbon materials have been proven to act as the defect-type less active sites for ORR via the two-electron pathway³¹. So, oxidized carbon materials can show good activity and selectivity for electrosynthesis of H_2O_2 by reducing O_2 via a 2e ORR³¹. These studies prompt us to explore possible synergistic effects by anchoring SACs on oxidized carbon supports to boost the electrochemical production of H_2O_2 via 2e ORR.

Herein, we report an innovative approach to a class of SACs with single Co atoms anchored on graphene oxide of Co-O-C active centers (i.e., Co-O-C@GO, designed as Co_1 @GO for simplicity) with a high Co mass loading up to 1.8% with atomic dispersion. These single Co atoms form a Co-O bond with a bond length of 1.47 Å, resulting in a sufficiently high oxidation state for the Co sites for oxygen reduction via a two-electron pathway. As a result, the newly developed Co_1 @GO exhibited an excellent 2e ORR activity with an onset potential of 0.91 V and a high selectivity of 81.4% for H_2O_2 production. Of particular importance, the H_2O_2 yield of Co_1 @GO is 1.0 mg cm⁻² h⁻¹, which is a 19-fold enhancement compared with GO and about 2-fold improvement compared with Co nanoparticles/GO. Our combined experimental observations and density functional theory (DFT) calculations indicate that the high reactivity and selectivity of Co_1 @GO for electrogeneration of H_2O_2 is arising from the Co-O-C active center with synergistic effects between the O-bonded single Co atoms and adjacent oxygen functional groups (C-O bond) of the GO.

Results and discussion

The synthesis and structural characterization of Co_1 @GO.

Co_1 @GO was synthesized through acid leaching of Co nanoparticles (Co NPs/GO) (Figs. 1 and 2a and Supplementary Fig. 1), in which Co nanoparticles (~1.9 nm) were acid etched into Co clusters (Co clusters/GO) (Supplementary Fig. 2) and then etched into single Co atoms and stabilized by oxygen functional groups of the GO (Supplementary Fig. 3), leading to a stable Co_1 @GO electrocatalyst. It can be seen that the intermediate Co clusters/GO possesses Co clusters and single Co atom (Co_1) (Supplementary Fig. 2c), though dominated by the Co clusters. The

presence of Co_1 suggested that part of Co clusters were dissolved by acid leaching to form single Co atoms, which were captured by the oxygen functional group of GO via Co-O bonding (Fig. 1). Further acid etching removed the Co clusters. High-angle annular dark field scanning transmission electron microscope images of Co_1 @GO are given in Fig. 2b, c and Supplementary Fig. 3, which show no Co NPs or Co clusters, but single Co atoms homogeneously interdispersed onto the GO support. Figure 2a, b reveals that Co clusters dissolved by acid leaching to form single Co atoms while Fig. 2c suggests that the resultant single Co atoms are stabilized on the GO support by Co-O bonding (vide infra). The energy-dispersive X-ray spectroscopy result in Supplementary Fig. S3c shows the presence of Co element in GO, further referring to the stability of single Co atoms anchored on the GO support. The X-ray diffraction (XRD) pattern of Co_1 @GO does not reveal additional diffraction peaks of Co apart from the typical broad peak centered around 24.9° from GO (Supplementary Fig. 4), indicating the successful transformation of the Co NPs to single Co atoms in Co_1 @GO (cf. Figs. 1 and 2 and Supplementary Figs. 1 and 2). The mass loading of Co in Co_1 @GO was determined by inductively coupled plasma–optical emission spectroscopic measurements to be about 1.8%. To investigate the GO structure of Co_1 @GO, we first performed the Raman spectroscopic measurements. As shown in Supplementary Fig. 5, the D band and G band of Co_1 @GO are at 1342.33 and 1587.49 cm⁻¹, respectively, similar to those for GO, which indicates that acid leaching did not cause an obvious change of the GO structure in Co_1 @GO^{32,33}. The Co 2p XPS spectrum of Co NPs/GO (Supplementary Fig. 6) could be separated into Co^{2+} (780.9 eV) to Co^{3+} (782.7 eV). The Co^{2+} (780.9 eV) state indicates that the surface of Co NPs has been oxidized into CoO. The Co^{2+} (781.1 eV) state of Co clusters/GO shows a positive shift of 0.2 eV compared with that of Co NPs/GO, which suggests that, after the HCl etching, the surface of Co clusters adsorbs hydroxyl (-OH). It could be confirmed that the C-O state of Co clusters/GO (533.5 eV) shows a down-shift of 0.2 eV compared with Co NPs/GO (C-O 1s, 533.7 eV), indicating that it has -OH on the surface of Co clusters and GO. The Co 2p XPS spectra of Co_1 @GO (Supplementary Fig. 6c) indicate that the Co atom site in Co_1 @GO is at Co^{2+} to Co^{3+} , suggesting the presence of Co-O bond. The high-resolution O1s XPS spectrum of Co_1 @GO (Supplementary Fig. 6f) shows three peaks: C-O-C (533.6 eV), C-O-H (532.5 eV) and C=O (531.1 eV). The C1s XPS spectra of these three samples also demonstrate the presence of C-O-C, C-O-H and C=O (Supplementary Fig. 6g–i). In addition, the ratio of C-O-C:C-O-H:C=O in Co NPs/GO, Co clusters/GO, and Co_1 @GO are 0.8:0.6:1, 1.7:1.4:1, and 2.3:1.5:1, respectively. The high content of C-O-C in Co_1 @GO suggests the high selectivity for H_2O_2 ³¹. Interestingly, the C-O-C bind energy in O1s peaks of Co_1 @GO is the lowest among these three samples, which indicated that the high oxide state of single-atom Co may contribute electron to the C-O, leading to the formation of a Co-O-C electron conjugated complex. The as-measured oxygen contents of Co NPs/GO, Co clusters/GO, and Co_1 @GO are 12.3%, 14.5% and 15.3%, respectively. The presence of the Co-O-C electron conjugated complex and the high oxygen content in Co_1 @GO suggests the high performance of two-electron pathway for ORR.

The presence of single Co atom on GO was further confirmed by X-ray absorption spectroscopic (XAS) measurements. The X-ray absorption near-edge structure spectra in Fig. 3a shows that the absorption edge intensity of Co_1 @GO is higher than that of Co foil and close to those of Co_3O_4 and CoO. In addition, the absorption edge peak position of Co_1 @GO is positively shifted compared with those of Co_3O_4 and CoO. These results indicate that Co is atomically dispersed in the Co_1 @GO, and that the Co center is coordinated with O atoms by interacting with oxygen

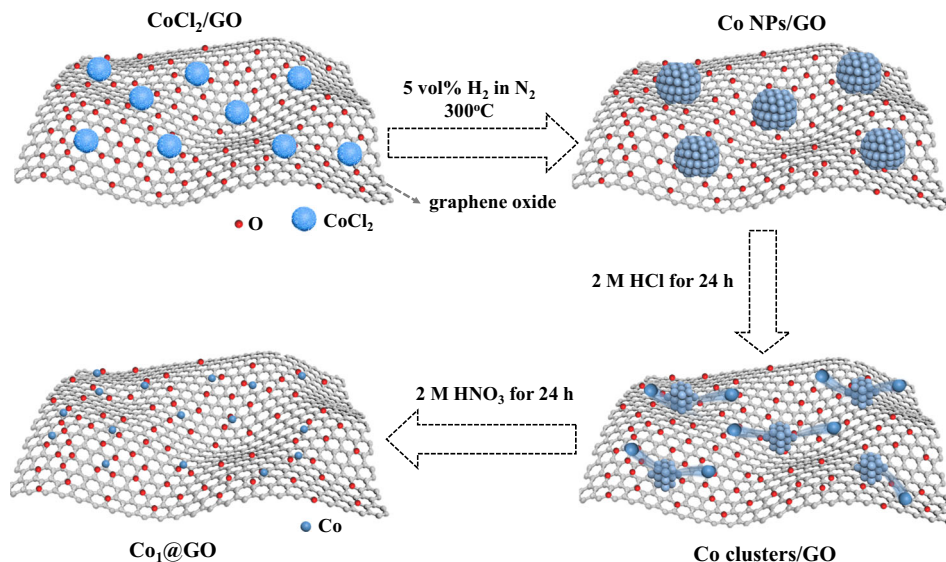


Fig. 1 Schematic of synthesis of $\text{Co}_1\text{@GO}$. Co nanoparticles were firstly prepared via reducing CoCl_2 in 5 vol% H_2 in N_2 (Co NPs/GO). Co NPs/GO was leached to form $\text{Co}_1\text{@GO}$.

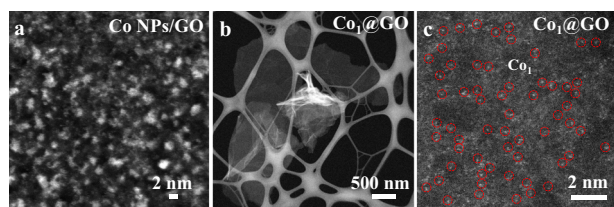


Fig. 2 Electron microscopy images. HAADF-STEM images of **a** Co NPs/GO and **b**, **c** $\text{Co}_1\text{@GO}$, with the red circle areas of Co_1 .

functional groups in the GO support to form the Co-O bond^{34–36}. The Fourier-transformed k^3 -weighted extended X-ray absorption fine structure spectra of $\text{Co}_1\text{@GO}$, Co_3O_4 , CoO , and Co foil are reproduced in Fig. 3b, which clearly show no notable peak from 2.0 to 3.0 Å for the Co-Co bond in $\text{Co}_1\text{@GO}$, but a prominent peak at 1.47 Å for the Co-O bond³⁷. Clearly, therefore, the Co NPs have been dissolved and remained as single Co atoms to coordinate with O (Co-O-C electron conjugated complex) from GO in the $\text{Co}_1\text{@GO}$ (Fig. 1 and Supplementary Fig. 1). Furthermore, the peak position at 1.47 Å is in good agreement with that of Co_3O_4 , suggesting that the Co atom sites in $\text{Co}_1\text{@GO}$ are at a high oxidation state³⁸, from +2 to +3, which should show higher activity than that of a low oxidation state³⁹. This result is in agreement with the XPS results, suggesting high electrochemical performance for $\text{Co}_1\text{@GO}$ (vide infra). The fitting results of the R space in Fig. 3c and the k-space in Supplementary Fig. 7 are consistent with the Co-O₃-C structure in DFT calculation results (vide infra), and also indicate the existence of the Co-O-C electron conjugated complex in the $\text{Co}_1\text{@GO}$.

The electrochemical performance of H_2O_2 . To investigate the electrochemical performance of single Co atom sites and the possible influence of the oxygen functional group in $\text{Co}_1\text{@GO}$, we performed the ORR measurements on $\text{Co}_1\text{@GO}$, Co NPs/GO and GO in 0.1 M KOH (Fig. 4) using a rotating ring-disk electrode (RRDE). Figure 4a reproduces the linear sweep voltammetry (LSV) curves for $\text{Co}_1\text{@GO}$, Co NPs/GO and GO in the 0.1 M KOH solution, in which the disk electrode detected the oxygen reduction currents while the Pt ring electrode monitored the yield of H_2O_2 . As can be seen, $\text{Co}_1\text{@GO}$ possesses a higher ORR

reactivity with an onset potential of 0.91 V versus a reversible hydrogen electrode (RHE) and a diffusion-limited current of ~ 0.5 mA, which are much higher than the corresponding values of 0.68 V and 0.028 mA for GO, 0.81 V and 0.34 mA for Co NPs/GO , and 0.76 V and 0.19 mA for Co clusters/GO (Supplementary Figs. 8 and 9). The high onset potential of $\text{Co}_1\text{@GO}$ is attributed to the synergistic effect between the O-bonded single Co atoms and adjacent oxygen functional groups (C-O bond) of the GO, which could decrease the free energy (-0.06 eV) of OOH^* (Fig. 5d). The low free energy could improve the reactivity of ORR performance, thus the enhanced onset potential. The production of H_2O_2 was quantified at 1.2 V by the Pt ring electrode, which avoided the ORR current on the ring with H_2O_2 oxidation only. Besides, Fig. 4a shows a much higher ring current for $\text{Co}_1\text{@GO}$ than those of GO and Co NPs/GO , indicating that the presence of single Co atoms also enhanced the yield of H_2O_2 . Figure 4b, c shows the selectivity and the yield of H_2O_2 , respectively, for $\text{Co}_1\text{@GO}$, GO and Co NPs/GO . As can be seen, the H_2O_2 selectivity of $\text{Co}_1\text{@GO}$, GO and Co NPs/GO are 81.4%, 76.3%, and 68.7% at 0.6 V, respectively. The observed relatively small change in the selectivity for these samples indicates that the C-O may be the important factor for the selectivity. In addition, the $\text{Co}_1\text{@GO}$ shows a H_2O_2 yield of $1.0 \text{ mg cm}^{-2} \text{ h}^{-1}$ at 0.50 V, which is 19-fold enhancements compared with GO ($0.052 \text{ mg cm}^{-2} \text{ h}^{-1}$) and about 2-fold improvement compared with Co NPs/GO ($0.55 \text{ mg cm}^{-2} \text{ h}^{-1}$). The observed big change in the H_2O_2 yield among these samples suggests that the Co-O is the main reason for the activity for the 2e ORR reactivity. These results indicate that single Co atoms on the GO support could enhance the 2e ORR reactivity and improve the H_2O_2 selectivity, simultaneously.

Importantly, $\text{Co}_1\text{@GO}$ also maintains a high H_2O_2 selectivity and activity when applied to a two-electrode system. In 0.1 M KOH, $\text{Co}_1\text{@GO}$ delivers a steady-state H_2O_2 at 0.76 V with corresponding to an H_2O_2 production rate of $\sim 5.7 \text{ mol g}^{-1} \text{ h}^{-1}$ or $28 \text{ mol m}^{-2} \text{ h}^{-1}$ (Supplementary Figs. 10 and 11). To our best knowledge, the onset potential and H_2O_2 production performance of $\text{Co}_1\text{@GO}$ are superior to most reported catalysts, such as $\text{Co}_1\text{@NG(O)}$ ($0.42 \text{ mol g}^{-1} \text{ h}^{-1}$)⁴⁰, Fe-CNT ($1.6 \text{ mol g}^{-1} \text{ h}^{-1}$)⁴¹ and Co-POC-O ($2.98 \text{ mol m}^{-2} \text{ h}^{-1}$)⁴² (Supplementary Table 1). Figure 4d, e presents the stability results, showing a disk and ring current of 0.32 and 0.024 mA, respectively, for $\text{Co}_1\text{@GO}$ at

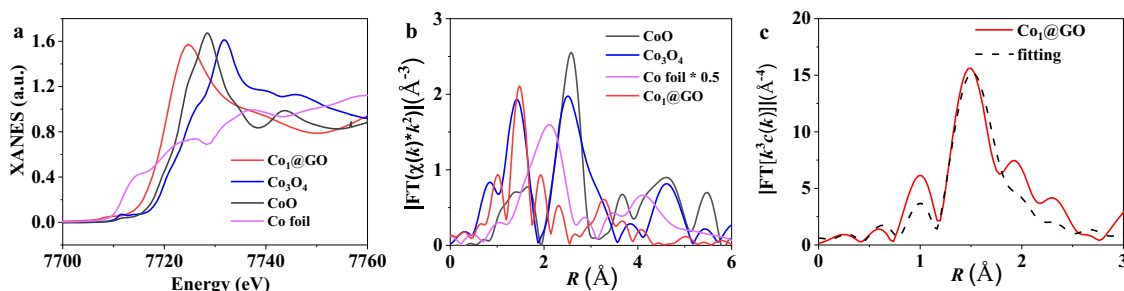


Fig. 3 X-ray absorption results of Co₁@GO. **a** XANES spectra and **b** Fourier transforms (FTs) of the Co K-edge of Co₁@GO, Co foil, CoO and Co₃O₄. **c** Corresponding fitting of the EXAFS spectra of Co₁@GO in R space.

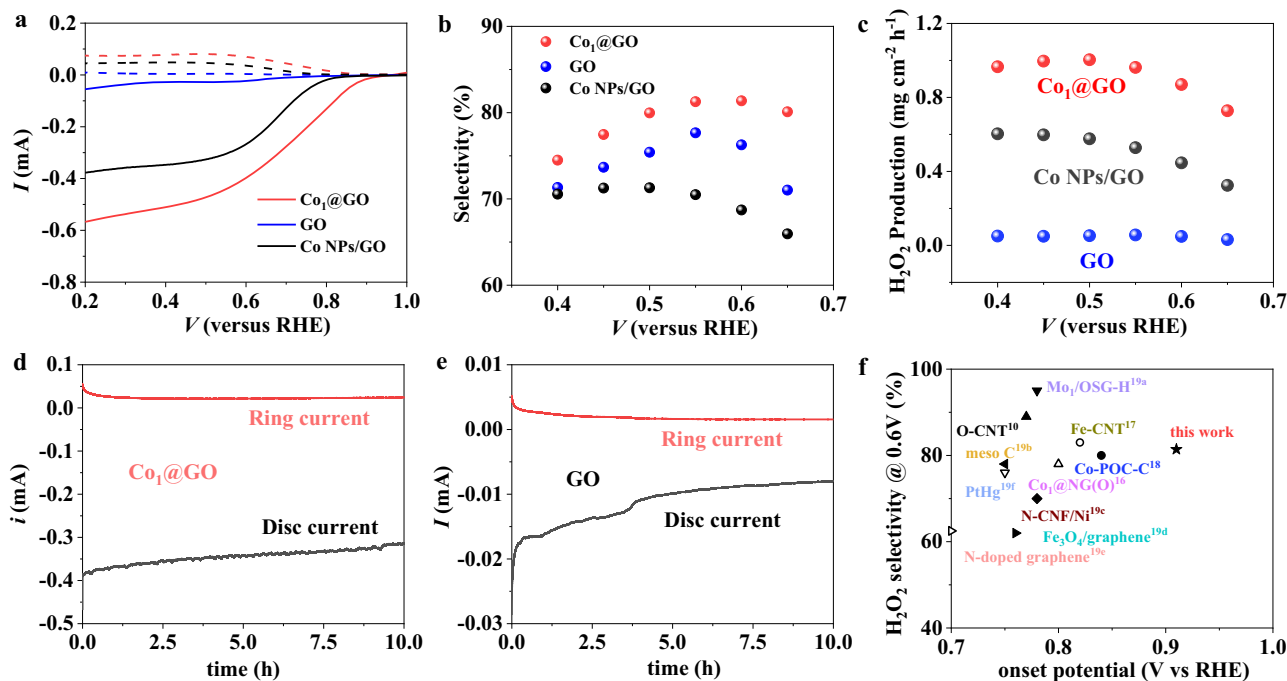


Fig. 4 Oxygen reduction performance of Co₁@GO and GO. **a, b** Oxygen reduction performance of Co₁@GO and GO in 0.1 M KOH at 1600 rpm (solid lines) and H₂O₂ product currents (ring electrode, dashed lines). **c** Electrosynthesis of H₂O₂ on Co₁@GO and GO in O₂-saturated 0.10 M KOH electrolyte. **d, e** Stability tests of Co₁@GO and GO at 0.1 M KOH. **f** Comparison of the onset potential and selectivity for electro-synthesis H₂O₂ on Co₁@GO and other reported catalysts at 0.6 V (RHE).

36,000 s, which are 40 and 3.6 times of the corresponding date for GO (disk current of 0.008 mA and ring current of 0.0067 mA). Clearly, therefore, Co₁@GO is a superb catalyst for the electrochemical generation of H₂O₂.

Figure 4f shows the onset potential versus the H₂O₂ selectivity for Co₁@GO, along with the corresponding data from various previously reported catalysts for comparison.^{31,40–50} As can be seen, Co₁@GO has the most positive potential with a relatively high H₂O₂ selectivity. For Co₁@GO, the high oxidation state of single Co atoms and oxygen functional group of GO in the Co-O-C electron conjugated complex contributed to the high reactivity and high selectivity for electro-synthesis of H₂O₂. As shown in Supplementary Fig. 12, Co₁@GO, Co NPs/GO, Co clusters/GO, and GO all show electron transfer numbers within the range of 2.3–2.7 over the potential from 0.4 to 0.7 V, indicating a 2e pathway for the oxygen reduction. The Co₁@GO maintains the lowest electron transfer numbers, demonstrating again that synergistic effects between the O-bonded single Co atoms and adjacent oxygen functional groups (C-O bond) of the GO in the Co₁@GO have significantly improved the kinetics for 2e ORR.

Clearly, therefore, anchoring single Co atoms of a high oxidation state onto a GO support could afford a feasible strategy to develop advanced electrocatalysts with excellent reactivity, high selectivity, and good stability toward electro-synthesis of H₂O₂.

Mechanistic investigation on H₂O₂ electrogeneration. To obtain a better understanding of the Co-O-C active centers and more insights into the catalytic mechanism of the Co₁@GO catalysts, we further performed DFT calculations (Supplementary Methods) to determine the free energy, overpotential, and reaction pathway for ORR on Co₁@GO. According to the experimental results for the coordination environment near the Co metal, the Co-O-C electron conjugated complex is detected as the active center in the Co₁@GO catalyst. Therefore, we built DFT models with possible Co-O structures (Supplementary Fig. 13 and Fig. 5a). With the DFT calculations, the catalytic center is identified as Co-O₃-C structure (Fig. 5a). The formation energy of this structure is -2.78 eV, indicating the thermodynamically spontaneous formation of the structures. The typical ORR cycle of four-electron pathway producing H₂O (A-B-C-D) and two-electron

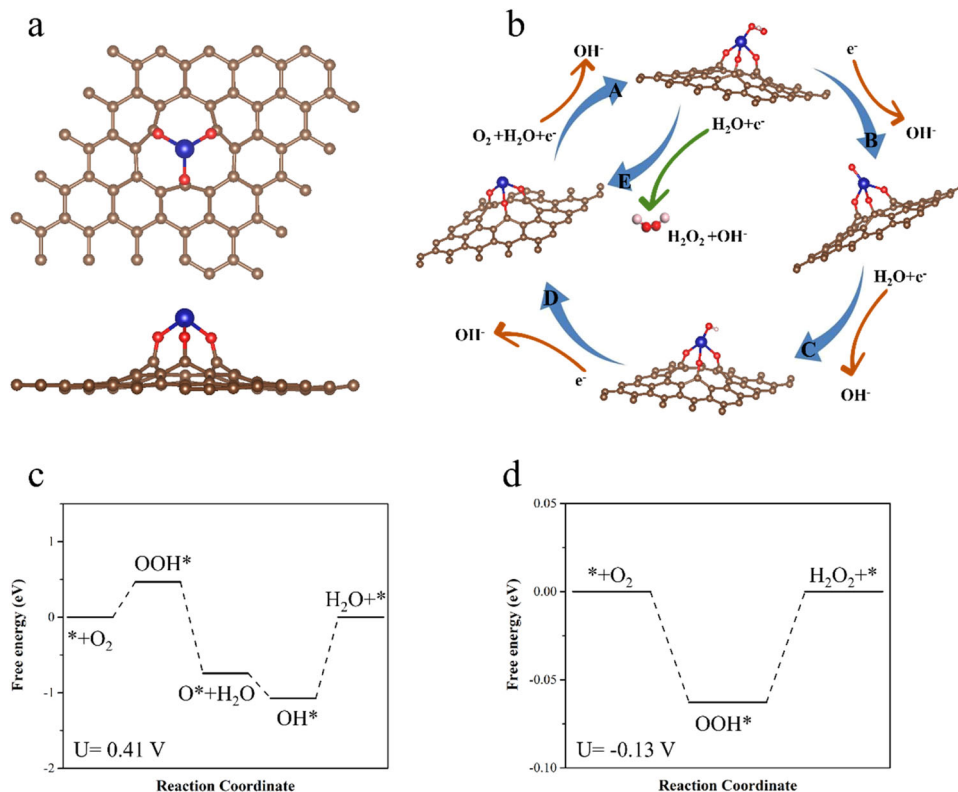


Fig. 5 Mechanistic investigation through DFT. **a** The model of Co-O₃-C structure used for DFT calculation. The brown, red and blue balls represent C, O and Co atoms, respectively. **b** The reaction cycle scheme of the intermediates in four-electron and two-electron ORR process on the Co-O₃ catalytic center. **c** Free energy diagrams of four-electron under equilibrium state ($U = 0.41$ V), and **d** free energy diagrams of two-electron ORR under equilibrium state ($U = -0.13$ V).

pathway producing H₂O₂ (A-E) on the Co-O₃ active center is illustrated in Fig. 4b. The free energy diagrams of four-electron and two-electron ORR for the Co-O₃-C structure are shown in Fig. 5c, d, respectively. For four-electron ORR, the reaction center shows a quite low catalytic activity with overpotential of 1.07 V. The rate-limiting step of four-electron ORR is identified to be the final step (OH* desorption), which is caused by the strong absorption of OH*. For two-electron ORR, the free energy change is extremely close to that of the ideal catalyst, and the overpotential is only 0.06 V, showing a high activity of producing H₂O₂. Thus, from the results of DFT calculations, the two-electron ORR is favored for the identified catalytic structure, consistent with the experimental results of high reactivity and selectivity of Co₁@GO for electroreduction of O₂ to H₂O₂ via a 2e pathway.

The free energy diagrams for Co-O₄-C structures (Supplementary Fig. 13) were also calculated and shown in Supplementary Fig. 14, and their formation energy and overpotential values considered are listed in Supplementary Tables 2 and 3, respectively. It is noted that the Co-O₄-C-(OH)₄ structure shown in Supplementary Fig. 13c also has good activity and selectivity of two-electron ORR toward H₂O₂, with four-electron overpotentials of 0.88 V and two-electron overpotential of 0.01 V, which is another possible active center. The density of states (DOS) and Bader charge distribution of the Co-O₃-C structure and other Co-O₄ structures are also analyzed and shown in Supplementary Figs. 15 and 16, respectively. In general, the metal ion Co in Co-O₄ structures carries a higher charge than that on Co-O₃ one, which may lead to stronger adsorption to the intermediates. The high electronic LDOS of the Co atom in Co-O₃-C structure is close to the Fermi level, promoting the electron transfer from the active center to the adsorbates during the reaction and leading to

unique two-electron ORR activity, whereas there is a large bandgap in the Co-O₄-C structures, which inhibits the electron transfer from the graphene sheet and consequently depresses the 2 electron ORR. Therefore, Co-O₃-C structure is more possibly the active center for H₂O₂ production via a 2e pathway for ORR.

Conclusion

In summary, we have demonstrated that high oxidation of single Co atoms anchored on a GO support (i.e., Co₁@GO) exhibited excellent performance for electrosynthesis of H₂O₂ from ORR via a 2e pathway. The newly developed Co₁@GO possessed a unique novel Co-O-C electron conjugated complex as the active center with synergistic effects between the O-bonded single Co atoms and adjacent oxygen functional groups (C-O bond) of the GO. Consequently, Co₁@GO delivered the highest reactivity and selectivity when compared with GO and reported catalysts (cf. Fig. 3) with good stability. DFT calculations confirmed Co-O₃-C as the catalytic center in Co₁@GO. This work represents a breakthrough in the electrosynthesis of H₂O₂ by rationally designing and developing highly effective, selective, and stable electrocatalysts with new active centers. The methodology developed in this study offers a novel and efficient approach for developing new electrocatalysts for various electrochemical reactions.

Methods

Synthesis of Co₁@GO samples. Co₁@GO was prepared through the dispersion of 6.2 mg CoCl₂ and 50 mg GO in Millipore water (18.2 MΩ·cm) under ultrasonication for 30 min (Ultrasonic baths, 480 W, Bandelin Electronic). The resultant mixture was freeze-dried (Alpha 1-2 LDplus Entry Freeze Dryer, Refrigeration system 0.43 kW, Martin Christ) for 48 h to remove water, followed by thermal treatment at 300 °C for 2 h in 5 vol% H₂ in N₂, forming Co nanoparticles (Co NPs/GO). The resultant powder was leached in 2 M HCl for 24 h, forming Co clusters

(Co clusters/GO), and then 2 M HNO₃ for 24 h to remove Co clusters. Finally, the sample was collected by centrifugation, washed with water and ethanol several times. The electrocatalyst thus produced was designated as Co₁@GO. For comparison, GO was prepared through the same procedure without the addition of CoCl₂.

Structural characterization. XRD results were recorded by a powder XRD (GBC MMA diffractometer) with Cu K α radiation at the scan rate of 2° min⁻¹. XPS spectra were recorded on Thermo ESCALAB250i XPS by using Al K α radiation, which was fixed in an analyzer transmission mode. The XAS results of Co K-edge were collected at an XAS station of the Beijing Synchrotron Radiation Facility. The morphological study of the newly developed catalysts was performed on a scanning TEM (JEOL ARM-200F, 200 keV).

Electrochemical measurements. The electrochemical performance of the resultant catalysts was carried out by using a three-electrode system at an electrochemical workstation (CHI 760 E, CH Instrument, USA). A Pt wire was used as the counter electrode and a saturated calomel electrode was applied as the reference electrode. The working electrode was using a RRDE. The ring electrode was Pt ring with an outside diameter of 0.75 mm and an inside diameter of 6.5 mm; the disk electrode was a glass carbon disk with a diameter of 5.0 mm. The slurry was prepared by adding 5.0 mg catalysts into a mixture of 50 μ L Nafion and 950 μ L ethanol, and then was sonicated for 1 h to form a homogenous dispersion. 5 μ L of the ink was dropped on the disk electrode. The working electrode was ready for testing after the solvent evaporated. The potential was calibrated to a RHE by applying the following equation:

$$E(\text{RHE}) = E(\text{SCE}) + 0.224\text{V} + 0.0592\text{pH}$$

All the tests were carried out in an O₂ saturated 0.1 M KOH solution at room temperature with a rotated rate of 1600 rpm. LSV was performed at a scan speed of 10 mV/s, and the potential of the ring electrode was set at 1.5 V (vs. RHE) to detect the production of H₂O₂. The selectivity, productivity, and electron transfer number were calculated by the following two equations:

$$\text{H}_2\text{O}_2 \text{ selectivity: H}_2\text{O}_2(\%) = 200 \times (i_r/N)/(i_d + i_r/N)$$

$$\text{H}_2\text{O}_2 \text{ productivity (mg cm}^{-2}\text{h}^{-1}\text{)} = 1/2 \times (i_r/N) \times M_{\text{H}_2\text{O}_2} \times 3600/(F/A)$$

$$\text{Electron transfer number } (n) = \frac{4i_r}{i_r + i_d/N}$$

i_r was the ring current and i_d was the disk current, N is the current collection efficiency of Pt ring electrode ($N = 0.26$), $M_{\text{H}_2\text{O}_2}$ is the molecular weight of H₂O₂ ($M_{\text{H}_2\text{O}_2} = 34.01 \text{ g mol}^{-1}$), F is Faraday constant ($F = 96485.3 \text{ C mol}^{-1}$), A is the area of disk electrode ($A = 0.196 \text{ cm}^2$). The collection efficiency of the electrode defined as the fraction of product from the disk to the ring is 0.26.

The stability test of these catalysts was performed by the chronoamperometric at a constant potential of -0.77 V (vs. RHE).

The bulk H₂O₂ production in 0.1 M KOH of Co₁@GO was conducted in an H-cell electrolyzer, with 0.5 mg cm⁻² Co₁@GO onto a 2 × 2 cm² Freudenberg GDL electrode (Fuel Cell Store) as the cathode, and Pt foil as the anode for H₂O electro-oxidation. A Fumasep FAA-3-PK-130 anion exchange membrane (Fuel Cell Store) was used to separate the chambers. The H₂O₂ concentration can be quantified by Ce(SO₄)₂ titration based colorimetric method ($2\text{Ce}^{4+} + \text{H}_2\text{O}_2 \rightarrow 2\text{Ce}^{3+} + 2\text{H}^+ + \text{O}_2$)³¹. The H₂O₂ concentration-absorbance liner was calibrated by adding certain amount of commercial H₂O₂ solution with 0.5 mM Ce(SO₄)₂. The Ce⁴⁺/H₂O₂ concentration was measured on a Cary 5000 UV-Vis-NIR spectrometer (Agilent) and the absorption at 320 nm wavelength was applied to determine its concentration.

Computational method. The DFT simulation on the free energies and overpotentials of two-electron ORR and four-electron ORR was carried out by DFT using the Vienna Ab initio simulation package (VASP)^{51,52}, where the soft projector-augmented wave and Perdew–Burke–Ernzerhof exchange correlation were implemented⁵³. The unit cells of the structures used in this study are composed of a single-layer graphene sheet embedded with Co and O atoms with the unit size set to 12.82 Å × 12.34 Å × 20.06 Å. Spin-polarization was considered in all calculations. The cutoff energy was set to 550 eV and the geometries were fully relaxed until the residual force convergence value on each atom being less than 0.01 eV Å⁻¹. The structures were sampled by a 3 × 3 × 1 k-point Monkhorst–Pack k-point mesh. In the calculation of reaction substrate and adsorbates, the implicit solvent effect is considered to simulate the aqueous environment by using the VASPsol code. Since Co is 3d-transition metal, the Hubbard U (DFT+U) corrections were also considered in the calculations⁵⁴.

Data availability

The data that support the findings of this study are available from the corresponding author upon reasonable request.

Received: 9 September 2021; Accepted: 7 February 2022;

Published online: 28 March 2022

References

- Yamanaka, I. & Murayama, T. Neutral H₂O₂ Synthesis by Electrolysis of Water and O₂. *Angew. Chem. Int. Ed.* **47**, 1900–1902 (2008).
- Shi, X. et al. Understanding activity trends in electrochemical water oxidation to form hydrogen peroxide. *Nat. Commun.* **8**, 701 (2017).
- Fukuzumi, S., Yamada, Y. & Karlin, K. D. Hydrogen Peroxide as a Sustainable Energy Carrier: Electrocatalytic Production of Hydrogen Peroxide and the Fuel Cell. *Electrochim. Acta* **82**, 493–511 (2012).
- Campos-Martin, J. M., Blanco-Brieva, G. & Fierro, J. L. G. Hydrogen Peroxide Synthesis: An Outlook beyond the Anthraquinone Process. *Angew. Chem. Int. Ed.* **45**, 6962–6984 (2006).
- Li, L. et al. Tailoring Selectivity of Electrochemical Hydrogen Peroxide Generation by Tunable Pyrrolic-Nitrogen-Carbon. *Adv. Energy Mater.* **10**, 2000789 (2020).
- Tang, C., Zheng, Y., Jaroniec, M. & Qiao, S.-Z. Electrocatalytic Refinery for Sustainable Production of Fuels and Chemicals. *Angew. Chem. Int. Ed.* **60**, 19572 (2021).
- Siahrostami, S. et al. Enabling direct H₂O₂ production through rational electrocatalyst design. *Nat. Mater.* **12**, 1137 (2013).
- Fukuzumi, S., Lee, Y.-M. & Nam, W. Solar-Driven Production of Hydrogen Peroxide from Water and Dioxygen. *Chem. – A Eur. J.* **24**, 5016–5031 (2018).
- Zhang, J., Chang, X., Luo, Z., Wang, T. & Gong, J. A highly efficient photoelectrochemical H₂O₂ production reaction with Co₃O₄ as a co-catalyst. *Chem. Commun.* **54**, 7026–7029 (2018).
- Jiang, K. et al. Highly selective oxygen reduction to hydrogen peroxide on transition metal single atom coordination. *Nat. Commun.* **10**, 3997 (2019).
- Melchionna, M., Fornasiero, P. & Prato, M. The Rise of Hydrogen Peroxide as the Main Product by Metal-Free Catalysis in Oxygen Reductions. *Adv. Mater.* **31**, 1802920 (2019).
- Kulkarni, A., Siahrostami, S., Patel, A. & Nørskov, J. K. Understanding Catalytic Activity Trends in the Oxygen Reduction Reaction. *Chem. Rev.* **118**, 2302 (2018).
- Lu, S., Jin, Y., Gu, H. & Zhang, W. Recent advances in active sites identification and regulation of M-N/C electro-catalysts towards ORR. *Sci. China Chem.* **60**, 999 (2017).
- Raj, C. R. et al. Emerging new generation electrocatalysts for the oxygen reduction reaction. *J. Mater. Chem. A* **4**, 11156 (2016).
- Edwards, J. K. et al. Switching Off Hydrogen Peroxide Hydrogenation in the Direct Synthesis Process. *Science* **323**, 1037 (2009).
- Verdaguer-Casadevall, A. et al. Trends in the Electrochemical Synthesis of H₂O₂: Enhancing Activity and Selectivity by Electrocatalytic Site Engineering. *Nano Lett.* **14**, 1603–1608 (2014).
- Yao, Y. et al. Engineering the electronic structure of single atom Ru sites via compressive strain boosts acidic water oxidation electrocatalysis. *Nat. Catal.* **2**, 304–313 (2019).
- Liu, P. et al. Photochemical route for synthesizing atomically dispersed palladium catalysts. *Science* **352**, 797 (2016).
- Zhang, B.-W. et al. Atomic cobalt as an efficient electrocatalyst in sulfur cathodes for superior room-temperature sodium-sulfur batteries. *Nat. Commun.* **9**, 4082 (2018).
- Zhang, Q. et al. Direct insights into the role of epoxy groups on cobalt sites for acidic H₂O₂ production. *Nat. Commun.* **11**, 4181 (2020).
- Tang, C. et al. Tailoring Acidic Oxygen Reduction Selectivity on Single-Atom Catalysts via Modification of First and Second Coordination Spheres. *J. Am. Chem. Soc.* **143**, 7819 (2021).
- Yang, H. B. et al. Atomically dispersed Ni(I) as the active site for electrochemical CO₂ reduction. *Nat. Energy* **3**, 140–147 (2018).
- Tian, S. et al. Carbon nitride supported Fe₂ cluster catalysts with superior performance for alkene epoxidation. *Nat. Commun.* **9**, 2353 (2018).
- Han, A. et al. A Polymer Encapsulation Strategy to Synthesize Porous Nitrogen-Doped Carbon-Nanosphere-Supported Metal Isolated-Single-Atomic-Site Catalysts. *Adv. Mater.* **30**, 1706508 (2018).
- Zheng, Y. et al. Molecule-Level g-C₃N₄ Coordinated Transition Metals as a New Class of Electrocatalysts for Oxygen Electrode Reactions. *J. Am. Chem. Soc.* **139**, 3336–3339 (2017).
- Choi, C. H. et al. Tuning selectivity of electrochemical reactions by atomically dispersed platinum catalyst. *Nat. Commun.* **7**, 10922 (2016).
- Sa, Y. J. et al. A General Approach to Preferential Formation of Active Fe–N_x Sites in Fe–N/C Electrocatalysts for Efficient Oxygen Reduction Reaction. *J. Am. Chem. Soc.* **138**, 15046–15056 (2016).

28. Yin, P. et al. Single Cobalt Atoms with Precise N-Coordination as Superior Oxygen Reduction Reaction Catalysts. *Angew. Chem. Int. Ed.* **55**, 10800–10805 (2016).
29. Chen, Y. et al. Isolated Single Iron Atoms Anchored on N-Doped Porous Carbon as an Efficient Electrocatalyst for the Oxygen Reduction Reaction. *Angew. Chem. Int. Ed.* **56**, 6937–6941 (2017).
30. Han, Y. et al. Hollow N-Doped Carbon Spheres with Isolated Cobalt Single Atomic Sites: Superior Electrocatalysts for Oxygen Reduction. *J. Am. Chem. Soc.* **139**, 17269–17272 (2017).
31. Lu, Z. et al. High-efficiency oxygen reduction to hydrogen peroxide catalysed by oxidized carbon materials. *Nat. Catal.* **1**, 156–162 (2018).
32. Wang, S. et al. BCN Graphene as Efficient Metal-Free Electrocatalyst for the Oxygen Reduction Reaction. *Angew. Chem. Int. Ed.* **51**, 4209–4212 (2012).
33. Li, Y. et al. Nitrogen-Doped Graphene Quantum Dots with Oxygen-Rich Functional Groups. *J. Am. Chem. Soc.* **134**, 15–18 (2012).
34. Zang, W. et al. Single Co Atoms Anchored in Porous N-Doped Carbon for Efficient Zinc–Air Battery Cathodes. *ACS Catal.* **8**, 8961–8969 (2018).
35. Yan, H. et al. Atomic engineering of high-density isolated Co atoms on graphene with proximal-atom controlled reaction selectivity. *Nat. Commun.* **9**, 3197 (2018).
36. Zhang, B.-W., Wang, Y.-X., Chou, S.-L., Liu, H.-K. & Dou, S.-X. Fabrication of Superior Single-Atom Catalysts toward Diverse Electrochemical Reactions. *Small Methods* **3**, 1800497 (2019).
37. Okumura, T. et al. Depth-resolved X-ray absorption spectroscopic study on nanoscale observation of the electrode–solid electrolyte interface for all solid state lithium ion batteries. *J. Mater. Chem.* **21**, 10051–10060 (2011).
38. van Oversteeg, C. H. M., Doan, H. Q., de Groot, F. M. F. & Cuk, T. In situ X-ray absorption spectroscopy of transition metal based water oxidation catalysts. *Chem. Soc. Rev.* **46**, 102–125 (2017).
39. Gu, J., Hsu, C.-S., Bai, L., Chen, H. M. & Hu, X. Atomically dispersed Fe³⁺ sites catalyze efficient CO₂ electroreduction to CO. *Science* **364**, 1091 (2019).
40. Jung, E. et al. Atomic-level tuning of Co-N-C catalyst for high-performance electrochemical H₂O₂ production. *Nat. Mater.* **19**, 436–442 (2020).
41. Jiang, K. et al. Highly selective oxygen reduction to hydrogen peroxide on transition metal single atom coordination. *Nat. Commun.* **10**, 3997 (2019).
42. Li, B.-Q., Zhao, C.-X., Liu, J.-N. & Zhang, Q. Electrosynthesis of Hydrogen Peroxide Synergistically Catalyzed by Atomic Co–N_x–C Sites and Oxygen Functional Groups in Noble-Metal-Free Electrocatalysts. *Adv. Mater.* **31**, 1808173 (2019).
43. Tang, C. et al. Coordination Tunes Selectivity: Two-Electron Oxygen Reduction on High-Loading Molybdenum Single-Atom Catalysts. *Angew. Chem. Int. Ed.* **59**, 9171–9176 (2020).
44. Feng, Y. et al. Tuning the catalytic property of nitrogen-doped graphene for cathode oxygen reduction reaction. *Phys. Rev. B* **85**, 155454 (2012).
45. Verdager-Casadevall, A. et al. Trends in the Electrochemical Synthesis of H₂O₂: Enhancing Activity and Selectivity by Electrocatalytic Site Engineering. *Nano Lett.* **14**, 1603–1608 (2014).
46. Chen, S. et al. Defective Carbon-Based Materials for the Electrochemical Synthesis of Hydrogen Peroxide. *ACS Sus. Chem. Eng.* **6**, 311–317 (2018).
47. Buan, M. E. M. et al. Nitrogen-doped carbon nanofibers on expanded graphite as oxygen reduction electrocatalysts. *Carbon* **101**, 191 (2016).
48. Barros, W. R. P. et al. Oxygen reduction to hydrogen peroxide on Fe₃O₄ nanoparticles supported on Printex carbon and Graphene. *Electrochim. Acta* **162**, 263–270 (2015).
49. Chen, C.-Y. et al. Oxygen Reduction Reaction on Graphene in an ElectroFenton System: InSitu Generation of H₂O₂ for the Oxidation of Organic Compounds. *ChemSusChem* **9**, 1194–1199 (2016).
50. Siahrostami, S. et al. Enabling direct H₂O₂ production through rational electrocatalyst design. *Nat. Mater.* **12**, 1137 (2013).
51. Kresse, G. & Furthmüller, J. Efficiency of ab-initio total energy calculations for metals and semiconductors using a plane-wave basis set. *J. Comput. Mater. Sci.* **6**, 15–50 (1996).
52. Kresse, G. & Furthmüller, J. Efficient iterative schemes for ab initio total-energy calculations using a plane-wave basis set. *Phys. Rev. B* **54**, 11169 (1996).
53. Perdew, J. P., Burke, K. & Ernzerhof, M. Generalized Gradient Approximation Made Simple. *Phys. Rev. Lett.* **78**, 1396 (1997).
54. Lin, C.-Y., Zhang, L., Zhao, Z. & Xia, Z. Design Principles for Covalent Organic Frameworks as Efficient Electrocatalysts in Clean Energy Conversion and Green Oxidizer Production. *Adv. Mater.* **29**, 1606635 (2017).

Acknowledgements

This research was supported by the Australian Research Council (ARC, DP190103881 and FL190100126).

Author contributions

B.-W.Z. and L.D. conceived and designed the project. L.D., R.A., S.-X.D., Z.X., Y.D., and Y.-X.W. supervised the project. B.-W.Z. prepared the samples and did the electrocatalytic performance test. B.-W.Z. and S.-Q.C. performed the characterization and measurements. D.Z. and Z.X. performed the DFT calculations. B.-W.Z., T.Z., Z.X., and L.D. wrote the manuscript. All the authors discussed the results and commented on the manuscript.

Competing interests

The authors declare no competing interests.

Additional information

Supplementary information The online version contains supplementary material available at <https://doi.org/10.1038/s42004-022-00645-z>.

Correspondence and requests for materials should be addressed to Liming Dai.

Peer review information *Communications Chemistry* thanks Wei Zhang, Md Golam Kibria and the other, anonymous, reviewer(s) for their contribution to the peer review of this work.

Reprints and permission information is available at <http://www.nature.com/reprints>

Publisher's note Springer Nature remains neutral with regard to jurisdictional claims in published maps and institutional affiliations.



Open Access This article is licensed under a Creative Commons

Attribution 4.0 International License, which permits use, sharing, adaptation, distribution and reproduction in any medium or format, as long as you give appropriate credit to the original author(s) and the source, provide a link to the Creative Commons license, and indicate if changes were made. The images or other third party material in this article are included in the article's Creative Commons license, unless indicated otherwise in a credit line to the material. If material is not included in the article's Creative Commons license and your intended use is not permitted by statutory regulation or exceeds the permitted use, you will need to obtain permission directly from the copyright holder. To view a copy of this license, visit <http://creativecommons.org/licenses/by/4.0/>.

© The Author(s) 2022